

Numerical Investigation of an Axis Symmetric Ramjet Missile Intake at High Angle of Attack

*Sachingowda A.C¹, Dr. N.K.S. Rajan² Dr. Tharakeshwar T.K³

1. M.Tech. Student, Department of Mechanical Engg. SIT, Tumkur, Karnataka, India¹

2. Chief Research Scientist CGPL Department of Aerospace Engg, IISc, Bangalore, Karnataka, India²

3. Assistant Professor, Department of Mechanical Engg, SIT, Tumkur, Karnataka, India³

Abstract: In the recent years, missiles with air-breathing engines like ramjets/scramjets are becoming popular for long range applications due to their high specific impulse compared to rockets. In order to reduce the cost of these new system development, flow prediction using CFD methods are advantageous. Hence, the objective of the present study is to identify a suitable two equation turbulence model that can be used for the design optimization, by proper validation with experiment. In this regard, the flow characteristics of an axisymmetric supersonic inlet system at different angles of attack have been studied using a 3D compressible RANS solver and compared with the experimental study of Herman [6]. The axis symmetric ramjet intake model used consisted of a two-cone mixed compression design, designed at Mach number $M_A = 2.99$. The numerical model consisted of an advection scheme with difference-splitting method with the SST $k-\omega$ turbulence model. In specific, the intake flow field has been analyzed at on-design (0° angle of attack) and three angles of attack (6° and 12°) conditions, corresponding to a supercritical mode of operation. A downstream mass flow throttle with a throttling degree/ blockage ratio of about 30% has been used to achieve this mode of operation. The results show that the cone shocks are captured quite well in the simulation till 12deg AoA. but at higher AoA there exists some discrepancy in the prediction. As the angle of attack increases the flow non-uniformity increases because of the viscous BL and SWBLIs effect, as well as the flow separation due to the terminal normal shock.

Keywords: Angle of Attack, SWBLIs, Viscous BL.

1 INTRODUCTION:

Ramjet engine is the simplest form of air-breathing, the engine consisting of an air inlet, combustor, and exhaust nozzle. The Pressure distribution measurement for a series of the hemispherically blunted cone Edward W et.al.[1] 1952. The effect of Reynolds number on angle of attack with various geometric changes Henry R et.al.[2] 1954. The 0° angle of attack performance of two-dimensional inlet near Mach number 3 Richard R. Woollett et.al.[3]. The design conditions for axis symmetric and two-dimensional supersonic inlet and exits James F. et.al.[4]. The performance of a two-dimensional cascade inlet at a free-stream Mach number of 3.05 and at angles of attack of -3° , 0° , 3° , and 6° Richard R. Woollett et.al [5]. Investigate the performance, such as pressure recovery and mass flow for axially symmetric inlet models with different internal compressions are analyzed at the designed Mach number 3, in an angle of attack of the range of 0° to 30° Dirk Hermann et.al.[6]. Three-dimensional Navier-stokes simulation with two-equation turbulence models of intersection shock-waves/ turbulent boundary layer Dr. T.J. Coakley et.al [7]. The turbulence modeling for high speed flows in this case the $k-\omega$, SO and HC models and the $q-\omega$ models over predicted the separation extent while the $k-\omega$ and $k-\epsilon$, models under predicted it. The best overall agreement was given by the $k-\omega$ model T.J. Coakley et.al.[8].

From the above review of literature, the following points can be noted:

- The performance of intakes strongly depends on the shock structure and the SWBLIs occurring within the flow field. Hence, the numerical models required for the prediction of flow must accurately predict the characteristics of SWBLIs.
- A large number of turbulence model validation studies indicate that two equation turbulence models can efficiently predict the weak SWBLIs but for strong interactions there exists a deficiency in separation zone prediction. Out of different models, SST $k-\omega$, model is found to be more suitable for adverse flow field and SWBLI prediction.
- A very few research studies have applied SST $k-\omega$ models for intake flow prediction. As well as few studies have validated the turbulence modes for high angle of attack flow prediction.
- Even though effect of angle of attack on the fixed geometry intake performance is well known the exact quantification at very high angles of attack is experimentally carried out by Herman et.al [6]. This shows after a particular AoA the shock interactions lead to high mass spillage.

1.1 Motivation for the current study:

- The design and geometrical optimization for an IRR missile intake has been taken up at CGPL, IISc Bangalore. In this regard, the current work is focused to identify an efficient and low cost two equation turbulence model for CFD technique that can be used for the optimization of intake.

1.2 Scope of the study:

The exact scope of the current study are:

1. To numerically investigate the flow field and performance of an axis symmetric intake at different angle of attack
2. To validate the prediction capability of SST k-w model by comparing with detailed experiments of Herman et.al [6].

1.3 Flow Field for Ramjet Intake:

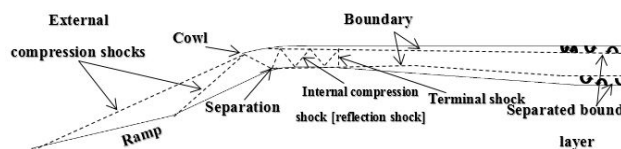


Fig. 1.1 Mixed compression intake flow field schematic

The schematic of a mixed compression ramjet intake is given in Fig. 1.1. This intake has the combination of both internal and external compressions. In the flow field, an external shock boundary layer interaction and as well as an interaction of cowl shocks and the center body boundary layer may cause flow separation dependent on the shock wave strength and also the nature of a forebody boundary layer.

The exact flow structure depends on the upstream flow condition and downstream combustion process.

2 Numerical Methodology:

Inlet model: An axis symmetric inlet model with mixed compression are considered for a free stream Mach number (shock on lip). The geometry is difference in their first [13°] and second [25°] cone angles and also internal compression for the higher angle of attack performance, with the cowl [15°]. For the high-pressure recovery, we consider two oblique shocks and a normal shock in the intake flow field.

Flow Conditions: The flow conditions specified with a free stream Mach number of $M_\infty=2.99$ and the total temperature of 105 K and correspondingly static pressure 0.68876 bar, velocity has 615 m s⁻¹. For this condition resulting in the Reynolds number of $2 \times 10^8 \text{ m}^{-1}$.

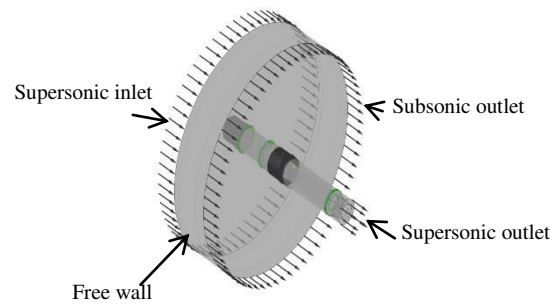


Fig. 2.1 Computational domains

2.1 Grid refinement and validation:

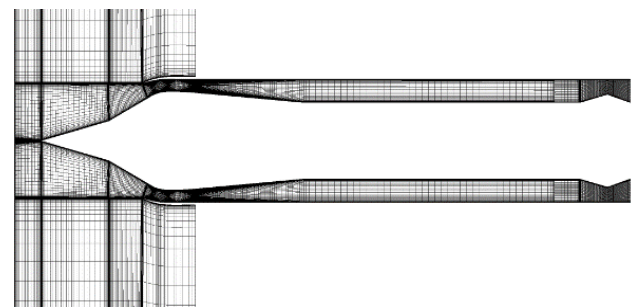
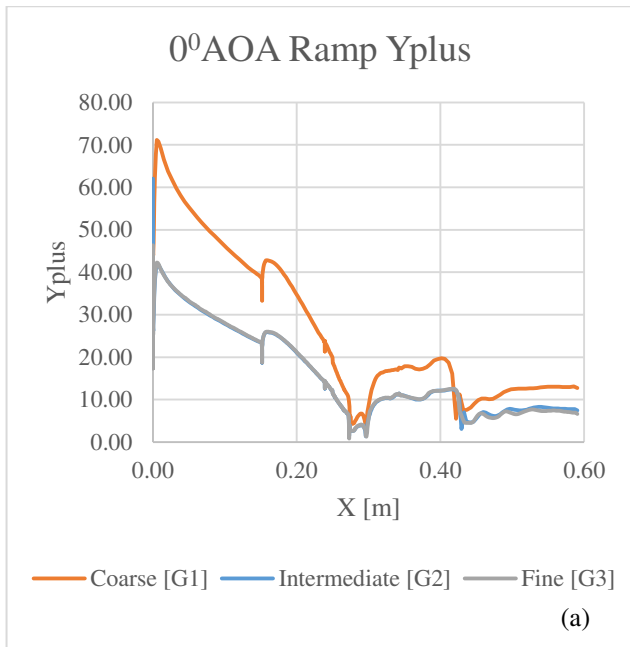


Fig. 2.2 Axis symmetric grid.

Table. 1 Grid independency values.

Level of the Resolution	Cells (millions)	First cell distance Y (mm)	Maximum wall Yplus
Coarse, G1	3.95	0.01	71
Intermediate, G2	7.05	0.005	43
Fine, G3	9.43	0.001	41



The above chart shows the variation of the ramp Y_{plus} v/s x -axis for the different level of the grid resolution. In this chart clearly shows Y_{plus} value is more coarse grid [G1], compared to intermediate grid [G2] and fine grid [G3], but intermediate grid [G2] and fine grid [G3] Y_{plus} values are the same. Therefore, intermediate grid [G2] is best because of a smaller number of cells compared the fine grid [G3] and difficulty to run big mesh, it takes more time to converge and big system required. That's why we choose the intermediate grid [G2] for analyses.

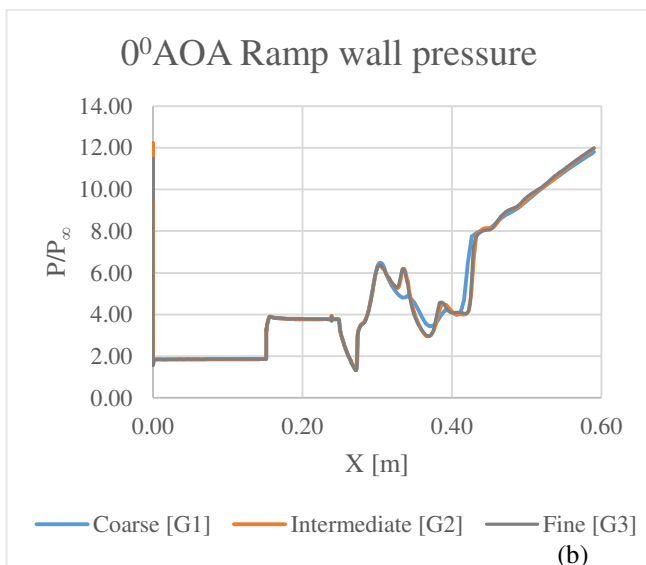


Fig. 2.3 (a) Ramp Y_{plus} , (b) Ramp wall pressure, for grid independence, $M_{\infty} = 2.99$, $AoA = 0^{\circ}$

The above chart shows the variation of the ramp pressure v/s x -axis for the different levels of the grid resolution. In this chart clearly, show ramp pressure values for intermediate grid [G2] and fine grid [G3] capture all the boundary of the intake compare to coarse grid [G1]. And the above chart shows the intermediate grid [G2] and fine grid [G3] are better ramp pressure distribution for overall ramp length. That's why we choose the intermediate grid [G2]. because of a smaller number of cells compared the fine grid [G3] and difficulty to run big mesh, it takes more time to converge and big system required.

3 Results and Discussion:

In this section, the detailed results of the numerical simulation of the axially symmetric ramjet intake considered for the study are presented. In specific, the intake flow field has been analyzed at on-design and three angles of attack (6° and 12°) conditions, corresponding to a supercritical mode of operation. At a different angle of attack conditions, as the internal flow-field of the intake becomes highly non-uniform, the following conventions shown in Fig. 3.1 are used to analyze the results

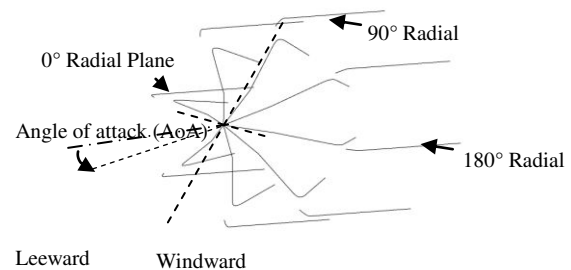


Fig. 3.1 Simplified illustration of windward and leeward side of the intake, notation for radial planes.

3.1 Effect of angle-of-attack on internal flow field:

3.1.1 One-design/ 0° angle-of-attack:

The internal flow field of the intake at the on-design condition of $M_{\infty} = 2.99$, 0° AoA and an exit blockage ratio of about 30% (corresponding to a back-pressure ratio of about 12), is presented in Fig. 4.2. This includes the contours of Mach number, streamlines and axial density gradient (numerical schlieren image). The shocks shown in the axial density gradient contour are thicker because of the numerical interpolation.

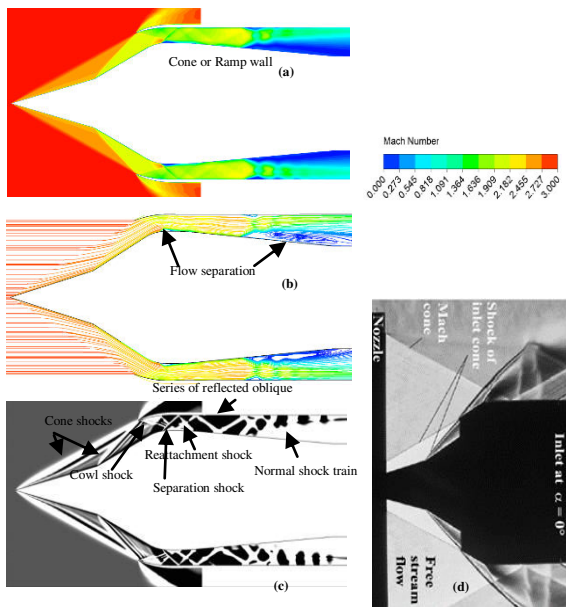


Fig. 3.2 Contours of (a) Mach number (b) Streamlines (c) Axial density gradient from computation, compared with the (d) Experimental schlieren photograph [6]; $M_\infty - 2.99$, $AoA - 0^\circ$.

The contours clearly shows that, as the flow enters the intake a bow shock is formed at the cone nose followed by the second cone shock across which the supersonic flow gets compressed. Both the shocks are incident just downstream of the cowl lip hence results in a complete capture of the incoming stream tube. The cone shocks then reflect back from the cowl surface and impinge at the throat, downstream of the compression cone/ramp corner inducing a small separation of the boundary layer.

In order to have a detailed quantitative analysis, the axial variation of ramp and cowl wall static pressure in the flow field compared with the results of MOC are presented in Fig. 3.3. Here, all the pressure data are non-dimensionalized by the freestream static pressure. The ramp wall pressure clearly indicates that at the beginning the pressure increases sharply across the bow shock at the cone tip, then reduces to a constant pressure ratio of 2 at the first cone. At the second cone, the pressure shows a further step increase due to the cone shock and remain constant before the flow expansion at the cone corner resulting in a dip in pressure. After this, the pressure increases across the cowl oblique shock boundary

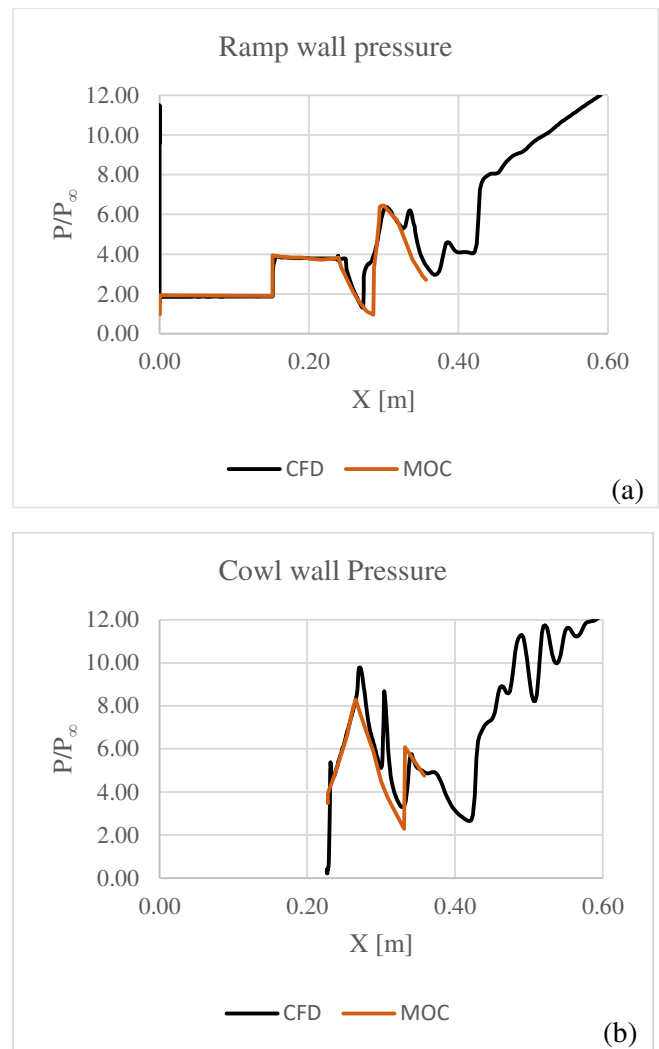


Fig. 3.3 (a) Non-dimensional ramp (b) Cowl wall static pressure distribution; $M_\infty - 2.99$, $AoA - 0^\circ$.

layer interaction. The comparison of pressure distribution with the result of MOC shows, all pressure peaks are predicted exactly with a small discrepancy near the flow separation zone ($x \sim 0.28$ m). This is because the MOC analysis doesn't take into account the viscous effect. Downstream, the pressure changes across the repeatedly reflected oblique shocks in the intake with a mean value decreasing in the diverging portion due to flow expansion. The sudden rise in the pressure close to $x \sim 0.42$ m occurs across the normal shock, thereafter the pressure increases monotonically till the exit of subsonic diffuser. The effect of the shock train is not reflected in the ramp pressure distribution as it is formed near the cowl wall.

The cowl wall static pressure can be explained in the same way, the sharp rise in pressure at the lip occurs across the two-cone shock and the strong reflected oblique shock. Then the pressure changes across the separation and reattachment shocks are impinging on the cowl wall separated by the expansion region. Downstream of this, the

pressure changes through the repeatedly reflected oblique shocks with a mean value decreasing in the diverging portion due to flow expansion similar to ramp pressure variation. At the location of normal shock, the pressure increases sharply then show a continuous rise and fall due to the presence of two secondary shocks in the shock train. The distribution clearly indicates that the majority of pressure increase occurs across the primary shock, the increase across the secondary shocks is low.

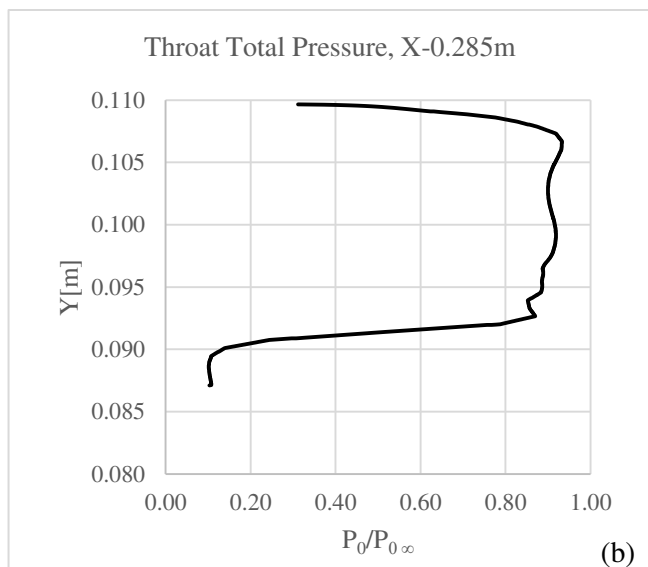
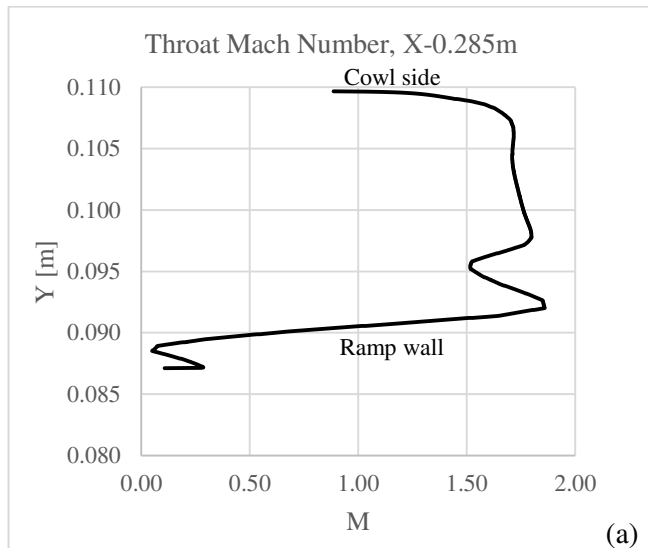


Fig. 3.4(a) Mach number (b) Non-dimensional total pressure distribution in the flow field at the throat ($x = 0.285$ m).

The variation of Mach number and total pressure at the throat section of intake ($x \sim 0.285$ m, from ramp to cowl side) are presented in Fig. 3.4. It clearly shows that almost a uniform flow field is established at the throat with an average Mach number close to 1.85 and stagnation pressure loss close to 10% of the freestream value. These changes in stagnation pressure and Mach number occurs across the

cone and cowl shocks as well as the ramp viscous BL. The average Mach number of 1.85, indicates that the flow field is completely supersonic at the throat. A closer look at the variation shows a dip in Mach number and stagnation pressure close to ramp side, is the loss across at the throat due to the SWBLIs.

3.1.2 6° angle-of-attack:

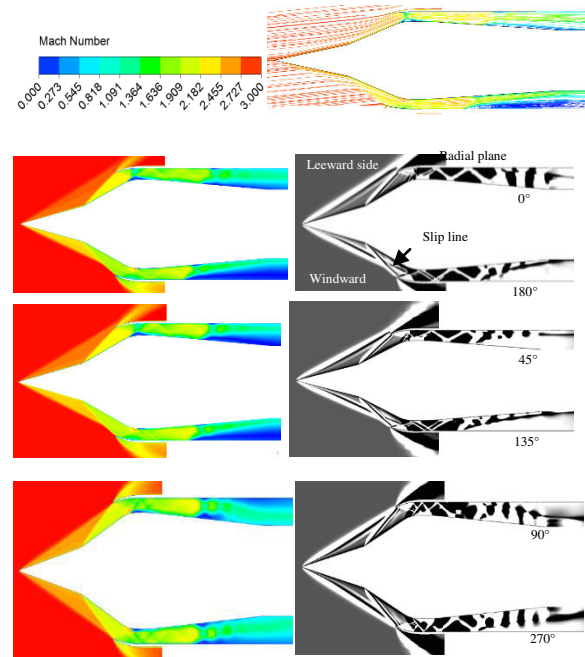


Fig. 3.5 Contours of (a) Mach number (b) Streamline (c) Axial density gradient from computation at different radial planes; $M_\infty = 2.99$, $AoA = 6^\circ$.

The comparison of schlieren images at different radial planes clearly shows that the cone shocks are not well focused on the cowl. Moving from the windward side to the leeward side as the effective cone angle seen by the freestream flow changes, the cone shock angles show a continuous change. Compared to the design condition, the windward side shocks are now closer to the cone surface, whereas the leeward side shocks are incident upstream of the cowl lip leading to spillage. The strong shocks produced on the windward side are shown to interact ahead of the cowl resulting in a slip line, which is directed into the intake. Hence, on the windward side, this slip line results in a mixing layer or disturbance close to the cowl wall.

The comparison clearly shows that till the throat the cone wall static pressure is maximum on the windward side, and keep decreasing towards the leeward side due to decrease in shock strength. But at the throat, the shock wave boundary layer interaction is the strongest in the leeward side leading to a higher pressure rise across it, whereas in the windward side the cowl shocks impinge further downstream of the cone corner hence the flow expansion at the cone corner is maximized. Downstream of the throat shock boundary layer

interaction, the changes in pressure contour clearly indicates, the repeatedly reflected shocks and the normal shock train positions are different from the windward side to the leeward side.

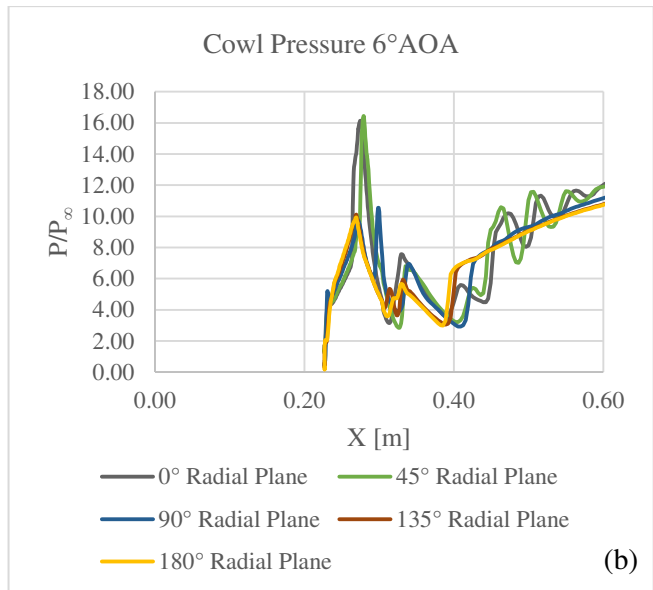
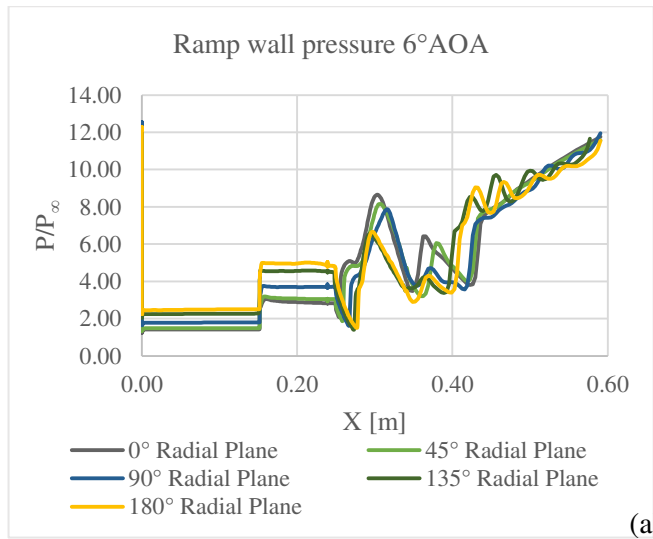


Fig. 3.6 (a) Non-dimensional ramp (b) Cowl wall static pressure distribution; $M_{\infty} - 2.99$, $AOA - 6^{\circ}$.

The cowl wall static pressure indicates the initial pressure rise close to the tip is higher in the leeward side because of the strong cowl shock, thereafter the flow pressure changes across the repeatedly reflected shocks and the normal shock train.

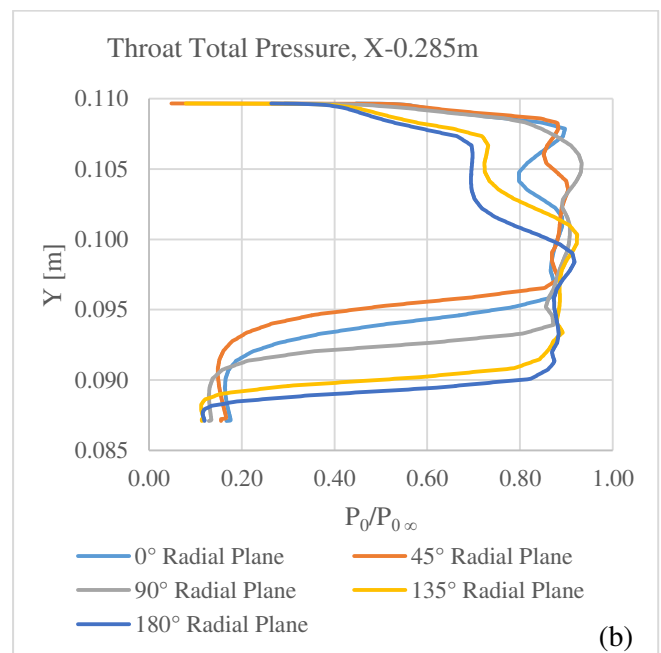
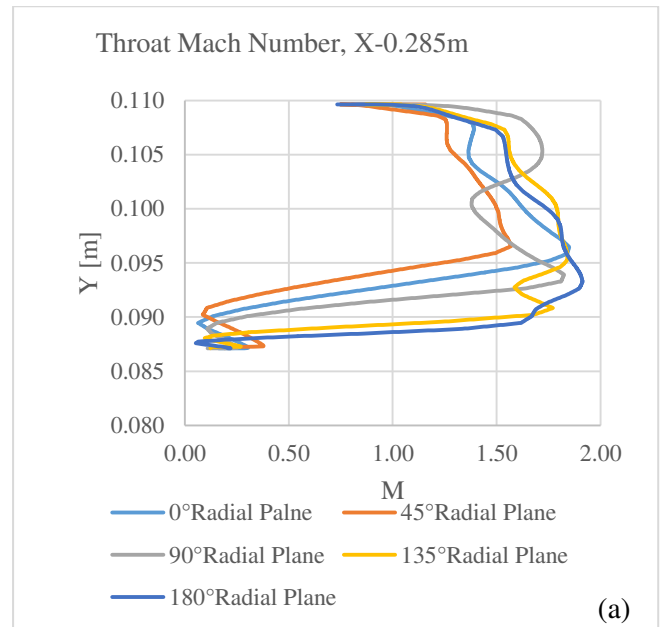
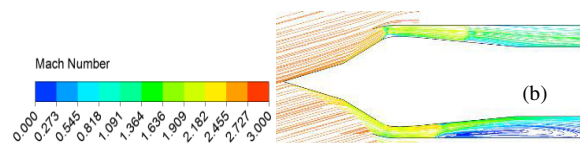


Fig. 3.7(a) Mach number (b) Non-dimensional total pressure distribution in the flow field at the throat (x - 0.285 m).

It clearly shows that almost a non-uniform flow field is established at the throat with an average Mach number varying from 1.5 to 1.9 along windward to leeward side. This is because of the change in shock system.

3.1.3 12° angle-of-attack:



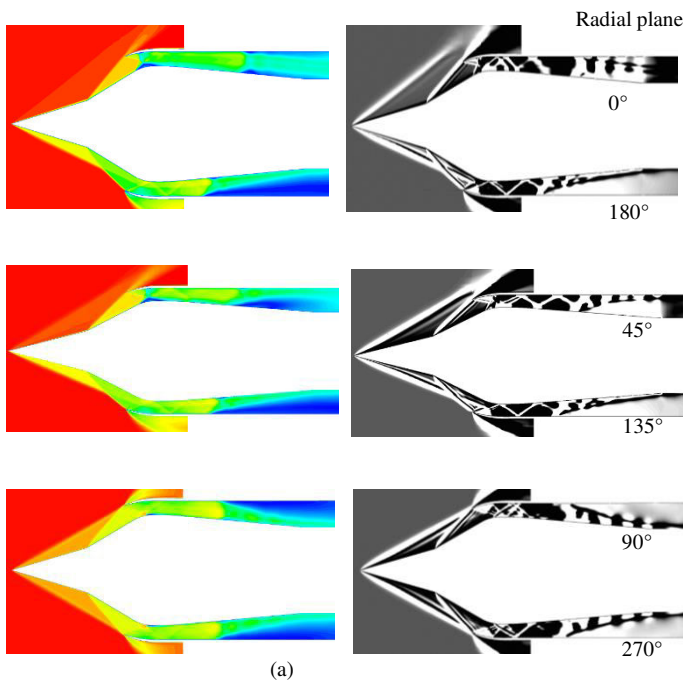


Fig. 3.8 Contours of (a) Mach number (b) streamline (c) axial density gradient from computation at different radial planes (d) experimental schlieren photograph [6]; $M_\infty - 2.99$, $\text{AoA} - 12^\circ$.

The comparison of schlieren images at different radial planes clearly shows that the cone shocks are not well focused on the cowl. Similar to the 6° AoA case, moving from the windward side to the leeward side as the effective cone angle seen by the freestream flow changes, the cone shock angles show a continuous change. In this case, the flow structure remains similar to the 6° AoA case except for a higher mass spillage in the leeward side and a strong shock interaction ahead of the cowl in the windward side.

A comparison with the experimental schlieren image indicates that the cone shocks are captured quite well in the simulation, as shown in Fig. 3.8 (c, d).

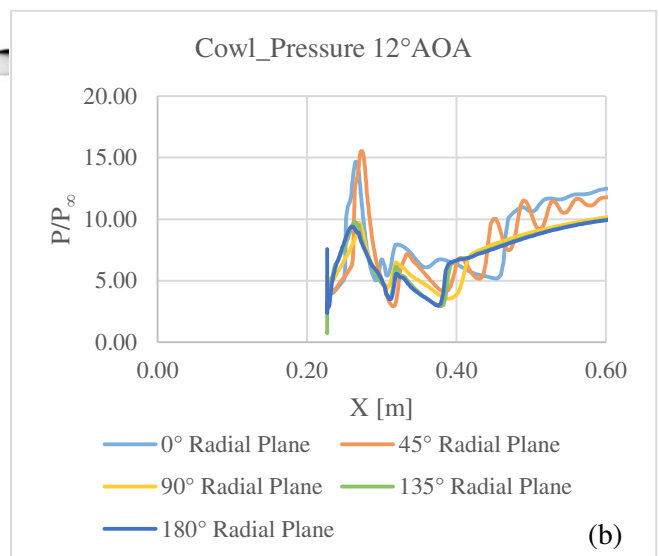
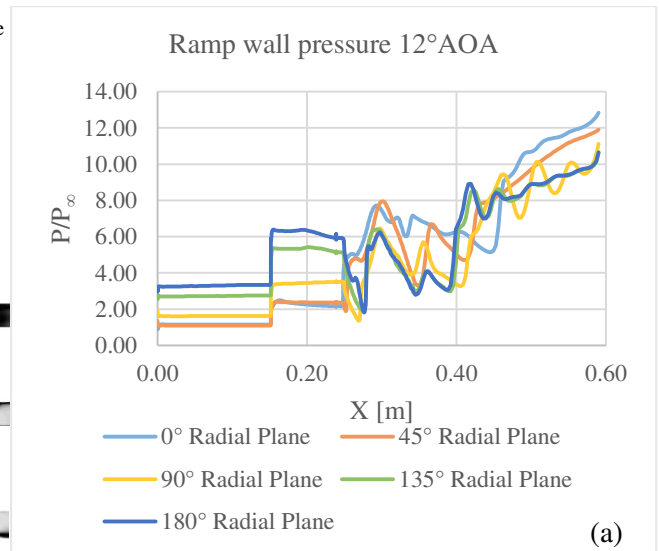


Fig. 3.9 (a) Non-dimensional ramp (b) cowl wall static pressure distribution; $M_\infty - 2.99$, $\text{AoA} - 12^\circ$.

As mentioned above, the variation of wall pressure is similar to the 6° AoA case. But the degree of non-uniformity increases with increase in angle of attack.

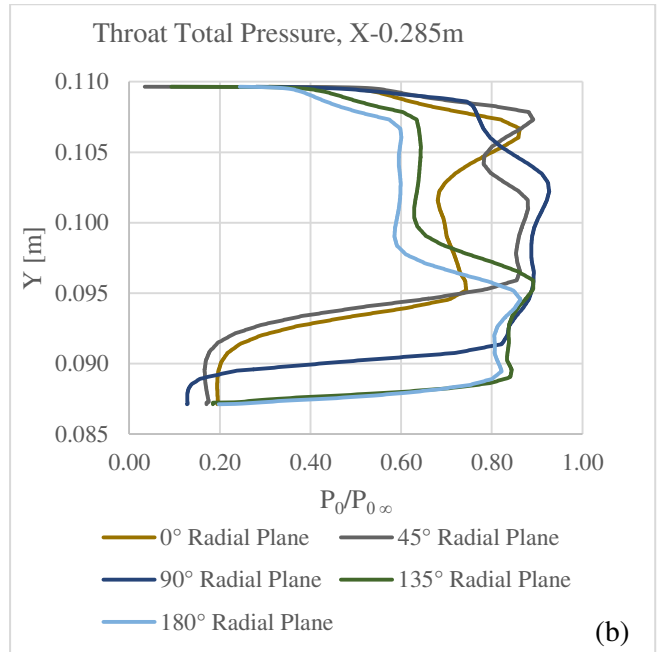
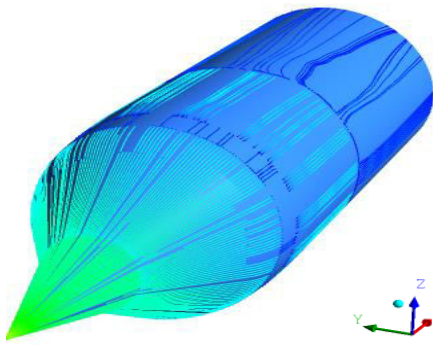


Fig. 3.10(a) Mach number (b) Non-dimensional total pressure distribution in the flow field at the throat (x – 0.285 m).

It clearly shows that a highly the non-uniform flow field is established at the throat stating from windward to leeward side.

3.2 Effect on Total pressure variation:

To have a better understanding of the flow field, the ramp surface streamlines and the total pressure variation at different cross-sections along the axial direction have been analyzed and presented.

3.3 0° angle-of-attack:

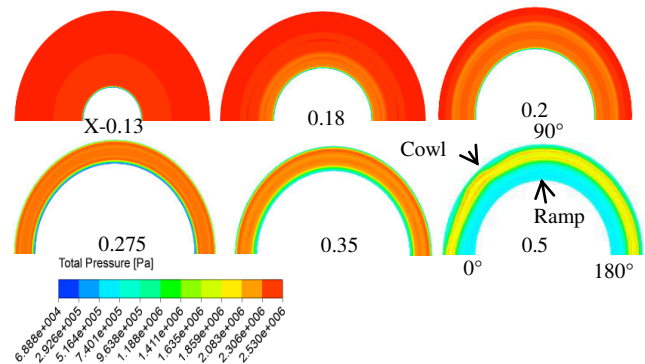
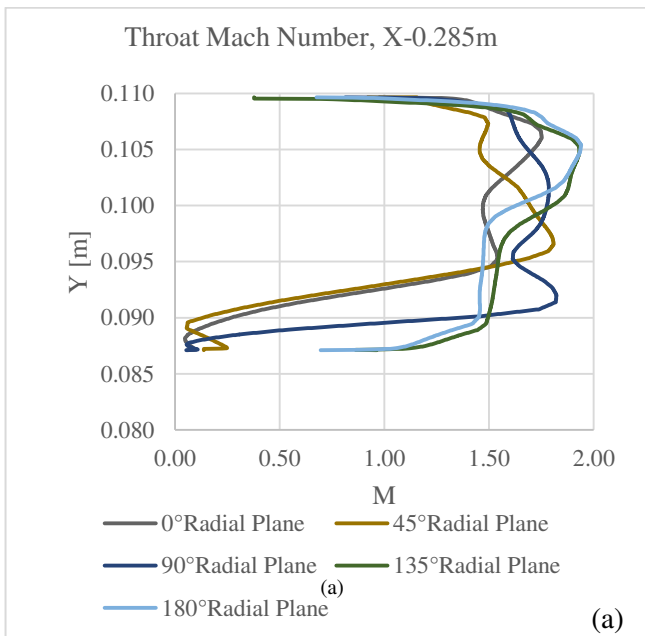


Fig. 3.11 (a) Contours of total pressure at different cross-sectional planes in the axial direction, (b) Surface streamlines on the ramp wall of the intake; $M = 2.99$, $\text{AoA} = 0^\circ$.

From both the contours clearly indicate that the flow field is completely axisymmetric. Starting from the cone tip to the cowl lip the reduction in stagnation pressure is small and is mostly because of the cone shocks. Downstream of the cowl, the loss occurs because of the SWBLIs and flow separation, resulting in low total pressure towards the exit of intake. At an axial location of $x \sim 0.5$ m near the subsonic diffuser, the fully sky-blue color indicates a low stagnation pressure region due to flow separation.

3.4 6° angle-of-attack:

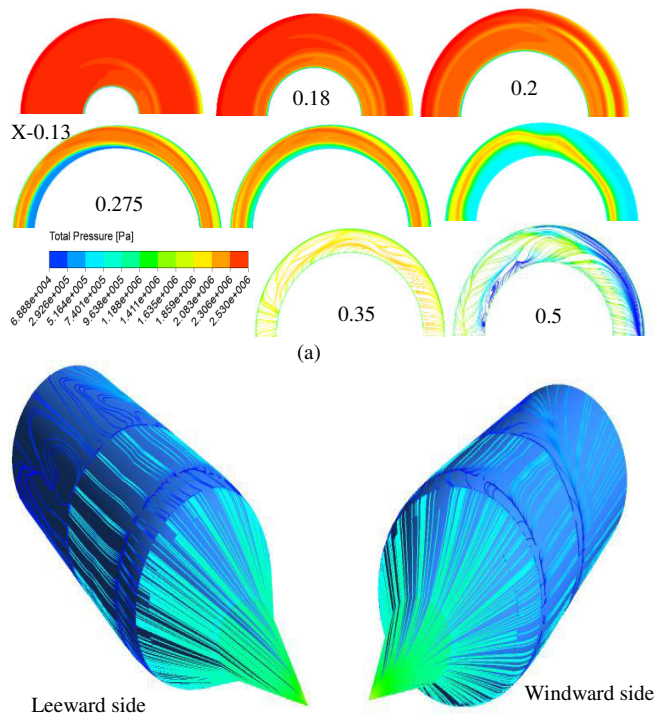


Fig. 3.12 (a) Contours of total pressure at different cross-sectional planes in the axial direction, (b) Surface streamlines on the ramp wall of the intake; $M = 2.99$, $\text{AoA} = 6^\circ$.

In the surface stream lines the flow starts to circulate from the windward side to the leeward side because of the high pressure in the windward side. This leads to a higher stagnation pressure in the subsonic diffuser close to the leeward side.

3.5 12° angle-of-attack:

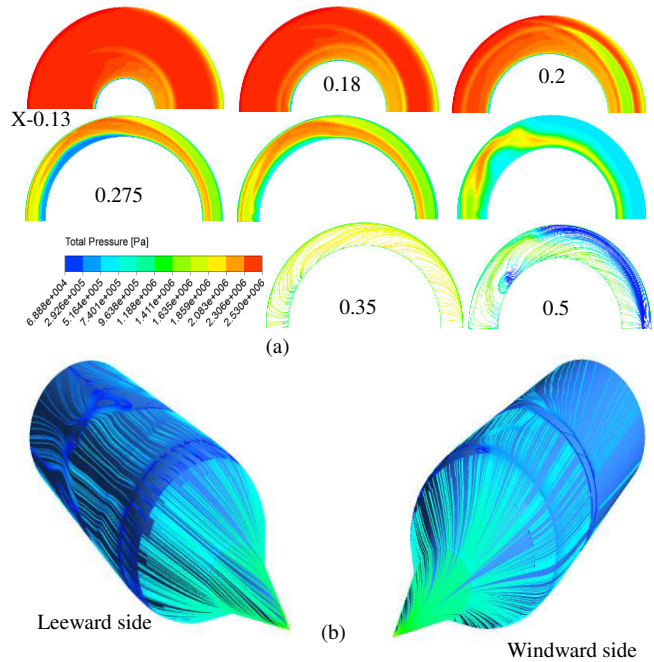


Fig. 3.13 (a) Contours of total pressure at different cross-sectional planes in the axial direction, (b) Surface streamlines on the ramp wall of the intake; $M = 2.99$, $\text{AoA} = 12^\circ$.

It clearly indicates a similar circulation of streamline from windward to leeward side. But due to higher strength of circulation in the flow field leads to the formation of two counter rotating vortices on the leeward side. This is clearly indicated in the stagnation pressure contours. Here, only half cross-section is shown with a single vortex.

3.6 Effect on Performance Parameters:

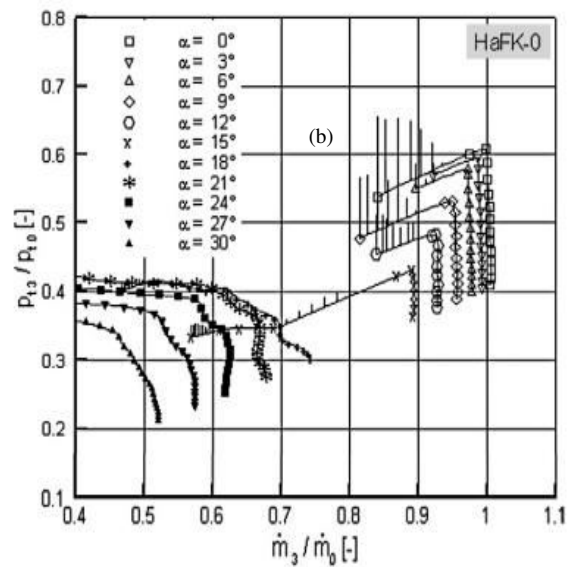


Fig. 3.14 Experiment results [6]

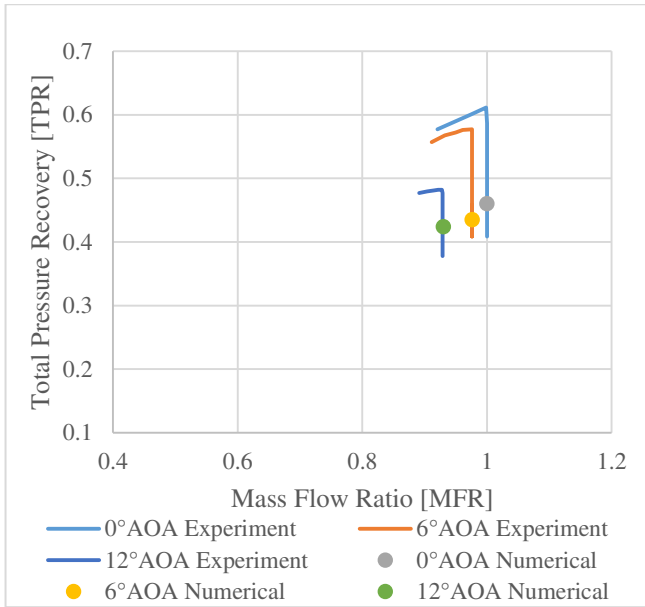


Fig. 3.15 Comparisons of numerical and experiment results [6].

The performance parameters obtained from the numerical simulation at EBR - 30% is given. As the angle-of-attack increased from 0° to 6° the mass flow ratio reduces by 3% and the total pressure recovery also reduces 3%. As angle-of-attack increases to 12° , there is 7% loss in mass flow ratio and 4% loss in total pressure recovery compared to 0° . The loss in mass flow ratio at high angle-of-attack increases due to the spillage.

3.6.1 Distortion Index:

The flow distortion at the exit of the intake increases with angle of attack. In order to quantify this, the exit flow Mach number and total pressure distribution have been compared and finally the flow distortion is quantified. And are presented below.

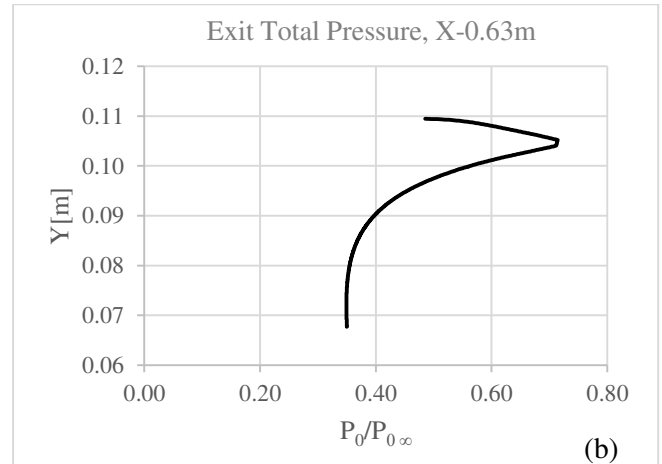
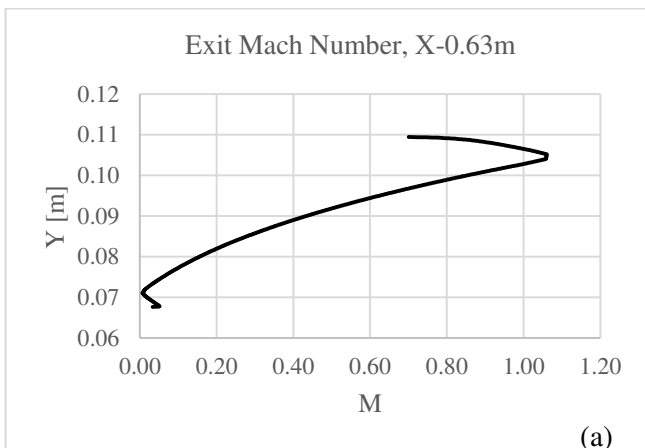
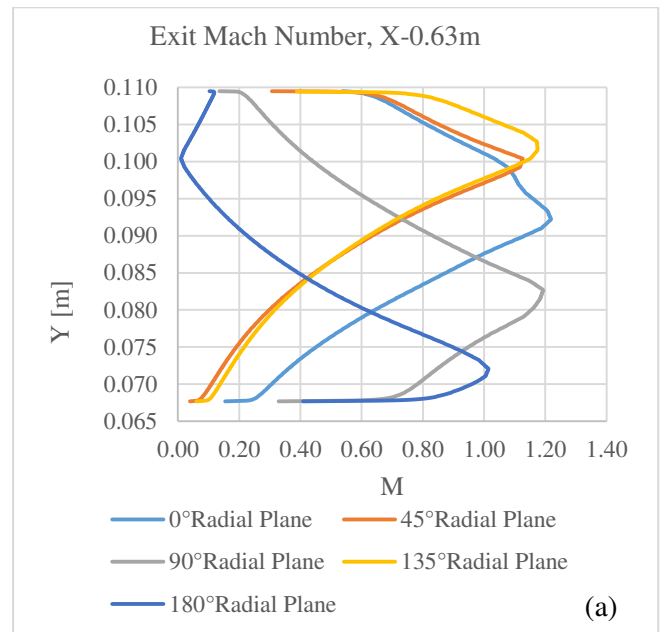


Fig. 3.16 (a) Mach number (b) Non-dimensional total pressure distribution in the flowfield at exit ($x = 0.63$ m) for 0° angle-of-attack.



(a)

(a)

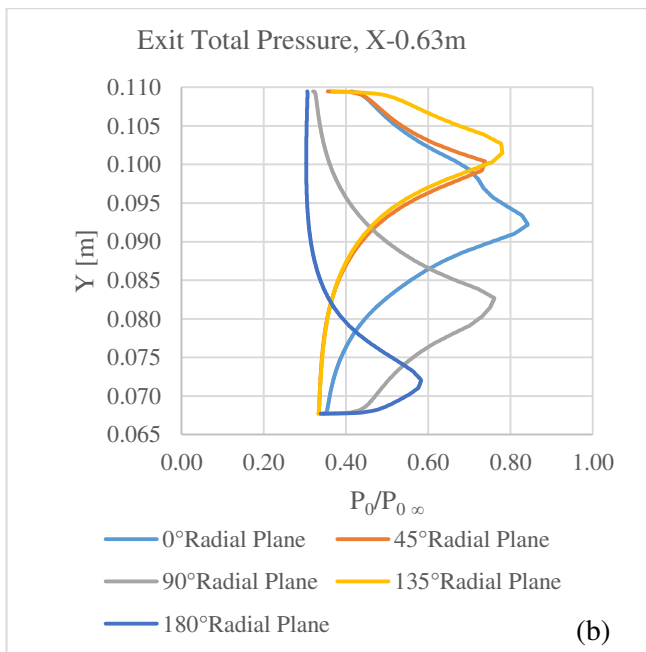


Fig. 3.17(a) Mach number (b) Non-dimensional total pressure distribution in the flow field at the throat ($x = 0.63$ m) for 6° AoA.

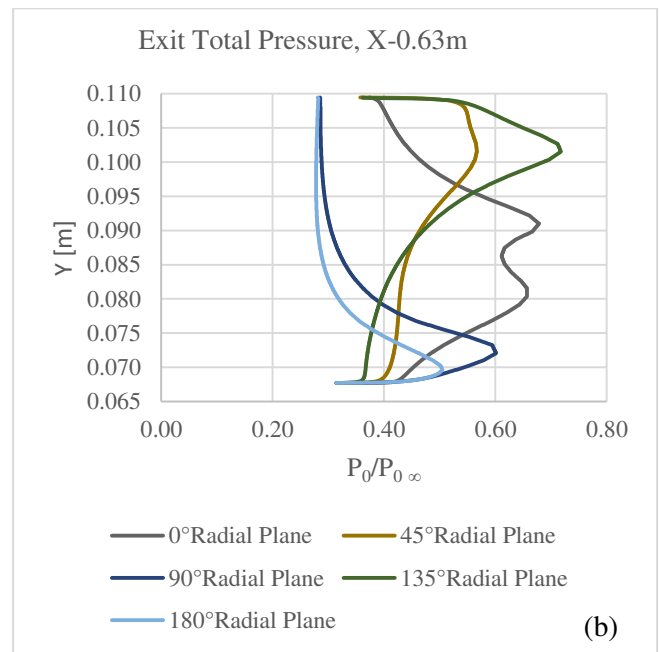


Fig. 3.18 (a) Mach number (b) Non-dimensional total pressure distribution in the flowfield at throat ($x = 0.63$ m) 12° AoA.

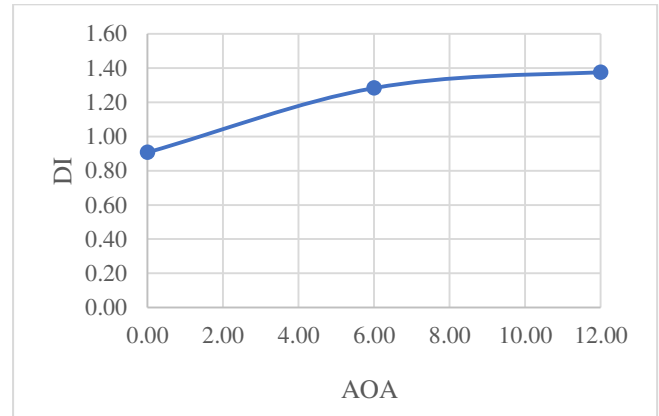
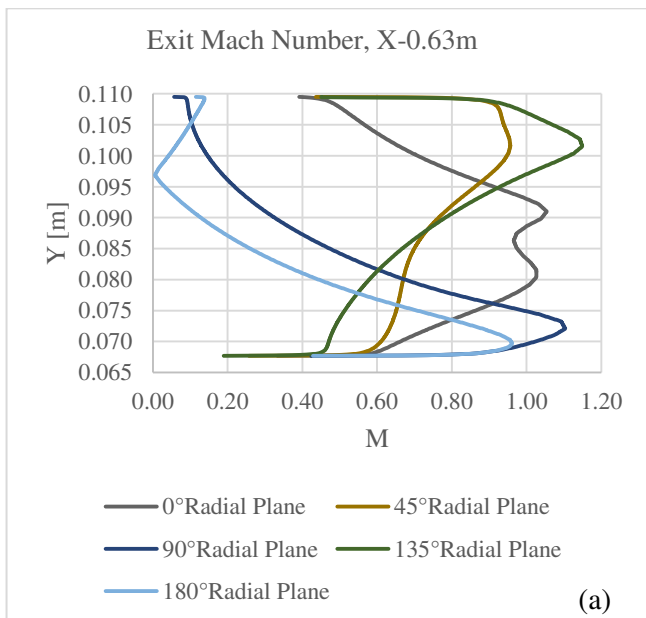


Fig. 3.19 Angle of attacks v/s Distortion index

The variation of distortion index with different angle-of-attack studied are presented in Fig. 3.19. The trend clearly shows that as the angle of attack increases the flow non-uniformity increases because of the viscous BL and SWBLIs effect, as well as the flow separation due to the terminal normal shock.

4 Conclusion:

1. The internal flow field for on-design and angle-of-attack till 12° are captured quite well in the computation. Hence the Mass flow capture performance is exactly predicted.
2. A comparison of axial density gradient from computation with the experimental schlieren image, for higher AoA indicates that cone shocks

and the normal shock are captured quite well, at the windward and leeward side of the intake

3. Up to 12° mass flow ratio and total pressure recovery are matching with the experimental results.
4. To have a better understanding of the flow field, the ramp surface streamlines and the total pressure variation at different cross-sections along the axial direction have been analyzed. It clearly indicates a circulation of streamline from windward to leeward side for different angle of attack.
5. The distortion index trend clearly shows that as the angle of attack increases the exit flow non-uniformity increases because of the viscous BL and SWBLs effect, as well as the flow separation due to the terminal normal shock.

For the future investigation, it is significant to

- (i) Find the best design model required for a higher angle of attack performances and also do analysis for higher angle attack till 30°
- (ii) To carry out analysis for peak pressure recovery prediction

References:

1. Edward W. Perkins and Leland H. Jorgengen: Investigation of the Drag of Various Axially Symmetric Nose Shapes of Fineness Ratio 3 for Mach Number from 1.24 to 3.67. NACARM A52H28, 1952.
<https://ntrs.nasa.gov/search.jsp?R=19930091022>
2. Hunczak, Henry R: Investigation of the Pressure Recovery and Mass-Flow Performance of Four Annular Nose Inlets Operating in Mach Number Region of 3.1 and Reynolds Number Range of Approximately 0.45×10^6 to 2.20×10^6 . NACA RA E54A07, 1954.
<https://ntrs.nasa.gov/archive/nasa/casi.ntrs.nasa.gov/19930090523.pdf>
3. Richard R. Woollett and James F. Connors: Investigation of the Zero-Angle-of-Attack performance of Two-Dimensional Inlet Near Mach Number 3. NACA RM E55K01, 1956.
<https://ntrs.nasa.gov/search.jsp?R=19930093760>
4. Connors James F and Meyer, Rudolph C: Investigation of the Design Criteria for Axisymmetric and Two-Dimensional Supersonic Inlet and Exits. NACA TN 3589, 1956.
<https://ntrs.nasa.gov/search.jsp?R=19930084405>
5. Richard R. Wollett and Harold M. Ferguson: Investigation of the Performance of Two-Dimensional CASCADE Inlet at A free-stream Mach Number of 3.05 and at Angles of -3° , 0° , and 6° . NACA RM E57L06. 1961.
<https://ntrs.nasa.gov/archive/nasa/casi.ntrs.nasa.gov/19930090011.pdf>
6. Dirk Hermann Klaus Triesch: Experimental investigation of the Inlet for High Agile Missiles Mach Number 3. Science Direct, 2006.
<https://doi.org/10.1016/j.ast.2006.05.004>
7. Patrick Brian Bookey: an experimental study of shock/turbulent boundary layer interaction at DNS accessible Reynold numbers, 2005.
8. Antonio Ferri and Louis M. Nucci: the origin of aerodynamic instability of supersonic inlet at subcritical conditions, Washington, 1951.
9. <https://www.cambridge.org/gb/academic/subjects/engineering/aerospace-engineering/shock-wave-boundary-layer-interactions?format=HB&isbn=9780521848527>